Full Length Article

Gas hydrate formation probability distributions: Induction times, rates of nucleation and growth

Peter J. Metaxas[a], Vincent W.S. Lim[a], Craig Booth[a], John Zhen[a], Paul L. Stanwix[a], Michael L. Johns[a], Zachary M. Aman[a], Gert Haandrikman[b], Daniel Crosby[c], Eric F. May[a,*]

[a] Fluid Science & Resources, School of Engineering, University of Western Australia, 35 Stirling Highway, Perth, WA 6009, Australia
[b] Shell Technology Centre Amsterdam, P.O. Box 3800, 1030 BN Amsterdam, Netherlands
[c] Shell Technology Center Houston, P.O. Box 432, 3333 Highway 6 South, Houston, TX 77210, USA

GRAPHICAL ABSTRACT
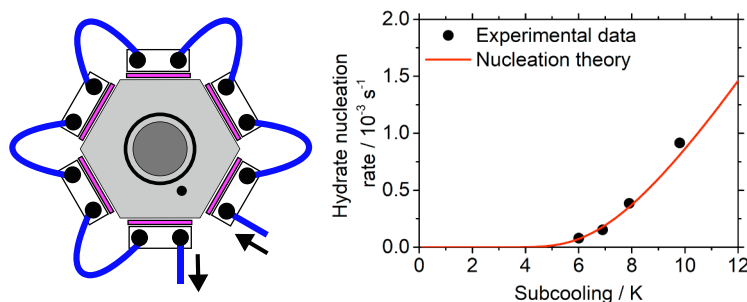
ARTICLE INFO

ABSTRACT

An improved, high pressure, stirred automated lag time apparatus (HPS-ALTA) was used to determine gas hydrate nucleation and growth rates from induction time measurements at fixed subcooling. The improved HPS-ALTA uses multiple thermoelectric elements to allow rapid, radially symmetric heating and cooling, which together with the automatic detection of hydrate formation, makes feasible the measurement of statistically significant induction time distributions. Four induction time probability distributions, with between 83 and 312 points, were measured at subcoolings ranging from (6 to 9.7) K for water with a synthetic natural gas mixture at pressures around 12 MPa. The induction time data measured at each subcooling were exponentially distributed and were fit using a model derived from Classical Nucleation Theory based on the mononuclear nucleation mechanism. The nucleation rates obtained in this work were consistent within a factor of three or better with recent literature measurements made using a completely different apparatus. Hydrate growth rates measured at fixed subcooling using the improved HPS-ALTA were also found to be stochastic but consistent with previous measurements of the kinetic growth rate in a binary gas mixture. The results obtained here establish the need to improve theoretical models of hydrate formation to reconcile predicted nucleation rates with the much slower ones observed experimentally.

* Corresponding author.
  E-mail address: eric.may@uwa.edu.au (E.F. May).

1. Introduction

Gas hydrates are ice-like solids in which gas molecules are enclathrated within a crystalline cage-like structure consisting of water molecules [1]. Natural gas hydrates can form under high pressure and low temperature and represent a significant challenge to the oil and gas industry since, once formed in a flowline, they can agglomerate and lead to flowline plugging. With subsea flowlines increasingly moving to deeper water to access newly discovered oil and natural gas fields, the risk of hydrate blockage is a primary concern to industry [2,3]. Rigorous characterisation of hydrate formation is a critical step to achieving a comprehensive understanding of hydrate blockage mechanisms necessary for the implementation of risk based hydrate management (versus complete hydrate avoidance) [4]. This is particularly the case for management strategies based on low dose hydrate inhibitors, where the selected chemical must undergo efficient and reliable performance qualifications [5]. Unfortunately, such characterisation is intrinsically challenging given the fact that hydrate nucleation is a stochastic process (i.e. non-deterministic); see, for example, the recent review of hydrate nucleation by Ke et al. [6]. This stochasticity necessitates a large number of repeat measurements to properly characterise hydrate formation probabilities and thus produce usable data for understanding hydrate formation risk and/or hydrate inhibitor chemical performance [7].

Obtaining a large number of hydrate formation measurements requires repeated cycling of system conditions into and out of the hydrate stability region. This enables hydrates to form and then dissociate prior to a subsequent measurement (see Fig. 1). Unfortunately, conventional tools for measuring hydrate formation (e.g. rocking cells and autoclaves) are typically not well suited to time-efficient temperature cycling. The limitations come from intrinsically large thermal masses of the measuring cell and/or cooling techniques which rely on changing the temperature of a liquid bath surrounding the measurement cell; such processes are typically limited to cooling rates of approximately $(1–6)\,K.h^{-1}$ [8,9]. This limits the rate at which the system conditions can, *via* changes in temperature, be moved into and out of the hydrate stability region, thereby limiting how quickly large numbers of formation events are obtained.
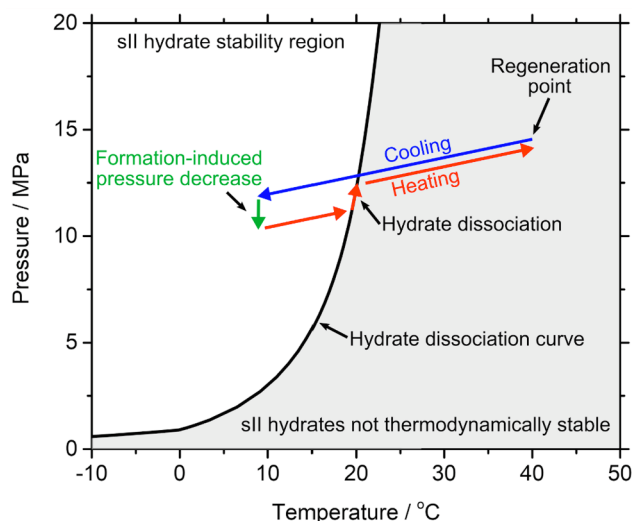
The development of small-volume automated lag time apparatuses (ALTAs) in the 1990s allowed for the acquisition of large numbers of ice or hydrate formation events in practical time frames (10–100 s of hours) thanks to the combination of automated detection and the ability to cool what were typically low volume systems at rates up to $4.5\,K.min^{-1}$ [10,11]. In later years, a high pressure ALTA (HP-ALTA) was developed which enabled studies of (e.g.) natural gas hydrate formation under elevated pressures [12–14] primarily as a function of subcooling $\Delta T = T_e–T$, where T_e is the hydrate equilibrium temperature at the formation pressure. However, the HP-ALTA typically yielded large subcoolings for hydrate formation even in chemically uninhibited systems. This was attributed at least in part to the liquid phase being quiescent [14]. Additionally, formation detection in the HP-ALTA was usually achieved through the detection of changes in the optical transmissivity of the sample, which limited the ability to study growth and also prevented discrimination between gas hydrate and ice.

In response to the aforementioned limitations, a high pressure, *stirred* ALTA (HPS-ALTA) was recently developed [7], which allows for the application of shear to the liquid phase during cooling and heating. Stirring is critical to minimise the mass-transfer limitations that can retard formation. Moreover, it uses a pressure-based detection method for hydrate formation, which not only allows for ice formation to be distinguished from hydrate formation but also enables growth rate characterisation. Using HPS-ALTA datasets consisting of over 500 hydrate formation events, May et al. [7] demonstrated the importance of shear in overcoming mass-transfer-limitations that can impede nucleation and growth. The system was also used to demonstrate how a kinetic hydrate inhibitor (KHI) not only increases the mean subcooling at which formation occurs but also could reduce (i) the degree of stochasticity and (ii) the initial hydrate growth rate. The large numbers of measured formation events allowed for the construction of high resolution probability distributions and, as a result, smooth cumulative hydrate formation probability distributions. This subsequently permitted comparisons between experimental data and predictions from hydrate nucleation theory [15].

In this work, we demonstrate the use of a 2nd generation HPS-ALTA (HPS-ALTA-2). The new apparatus has a higher volume, enabling larger liquid loadings (5 mL versus 1 mL). More importantly, however, the use of multiple thermoelectric elements (Fig. 2) enables faster and more uniform heating and cooling than the 1st generation apparatus. These fast temperature ramp rates enable target subcoolings as well as the

Fig. 1. Hydrate dissociation curve for the sII-hydrate-forming gas mixture under study in this work as calculated using the cubic-plus-association (CPA) model implemented in Multiflash 6.2 (see Section 2.2 for the composition of the gas mixture). This curve separates regions in pressure-temperature space where sII hydrates are thermodynamically stable and unstable. Large-headed arrows indicate the use of temperature ramping to repeatedly take a constant volume system into and out of the hydrate stability region where hydrate formation induces a drop in the gas phase pressure.
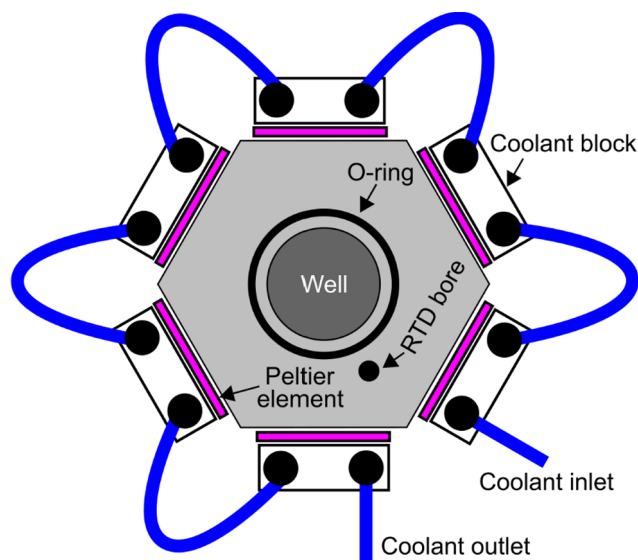

Fig. 2. Top-down, simplified schematic of an open HPS-ALTA-2 cell. For clarity, the recess in which the lid sits, and the bolt holes used to seal the lid, are not shown.

high temperature regeneration conditions (used to dissociate hydrates between measurement runs; see e.g. Fig. 1) to be reached faster in comparison with previous experiments. The total time needed to measure hydrate formation probability distributions is thus reduced significantly, thereby removing barriers that tend to prevent the collection of such datasets in practical time frames [16]. Fast ramping is particularly important to studies at high subcooling where induction times are short and thus comparable to or smaller than the time it would take to cool the system from the regeneration temperature using a conventional apparatus. If necessary, the data acquisition rate can be further increased by using multiple, identical HPS-ALTA-2 cells in parallel.

In contrast to the subcooling distributions measured by May et al. [7] *via* constant cooling experiments, in this work, we detail the use of a HPS-ALTA-2 cell for studies of induction times for hydrate formation at fixed temperature and pressure. The mononuclear nucleation mechanism of Classical Nucleation Theory (CNT) [17] predicts that, under such conditions, induction times are exponentially distributed with the cumulative probability, *P*, given as follows:

$$P(t) = 1 - \exp(-Jt) \tag{1}$$

where J is the nucleation rate and t is the time elapsed prior to nucleation. This relatively simple functional form for *P* (into which some authors introduce a lag time not considered by CNT) has been shown to apply to nucleation phenomena in a number of physical systems (e.g. [18–21]) including nucleation-controlled hydrate formation [8,16,22,23].

By fitting the subcooling-dependence of the observed formation rates using a theoretical model developed by Kashchiev and Firoozabadi through the application of CNT to gas hydrates [15], it is possible to extract estimates of the kinetic and thermodynamic nucleation parameters. The robust measurements of formation probability as a function of induction time at various fixed subcoolings achieved in this work provides the opportunity to test the applicability of the CNT framework to the description of hydrate nucleation.

2. Material and methods

2.1. Experimental apparatus

The HPS-ALTA-2 cell is a machined stainless steel pressure cell with a hexagonal external cross-section (Figs. 2 and 3a). The cell has a central cylindrical well with radius 1.2 cm and depth 2.4 cm, corresponding to a total cell volume of 10.9 mL. A nitrile o-ring, which serves to seal the cell, sits in a groove in the cell body and is compressed by the stainless steel lid. The region of the lid that covers the well contains a port for gas injection (Fig. 3b). The short gas injection line includes an in-line pressure transducer (DF2-SS-01-3000, DJ Instruments) and a valve to isolate the cell following pressurisation (15-11AF1, High Pressure Equipment Co.). A 1/8″ diameter, 100 Ω platinum RTD (resistance temperature detector; P-M series; Omega Engineering Inc.) is inserted through the lid into a bore within the wall of the cell and is used to monitor the temperature of the cell body (the bore is visible in Figs. 2 and 3a).

A Peltier element (12711-5L31-05CL-S; Custom Thermoelectric, LLC) is mounted on each of the six sides of each cell to enable heating and cooling of the cell. This arrangement enables more spatially symmetric heating and cooling than was possible with the first generation HPS-ALTA, which only had a single Peltier element on the cell's underside [7]. The Peltier elements are compressed between the cell body and water blocks (WBA-1.25-0.50-CU-NP, Custom Thermoelectric, LLC) through which a water-MEG coolant mixture flows, driven by a circulation chiller (MC 600, LAUDA-Brinkmann, LP). The cell temperature is controlled *via* a PID loop implemented in LabVIEW [24] which sets the voltage delivered to the Peltier elements by external power supplies. The RTD provides a measurement of the cell temperature for the PID loop. The apparatus allows for linear cooling ramps at rates, *β*, of up to
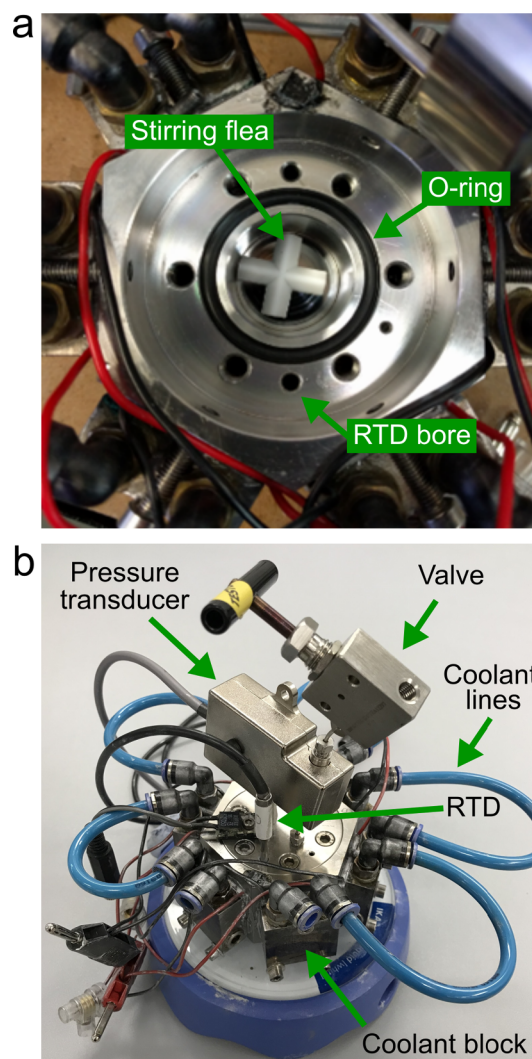
Fig. 3. (a) Top-down view of one of the HPS-ALTA-2 cells without the lid present. The image shows the cylindrical well surrounded by an o-ring groove, 6 threaded holes for securing the lid and 2 bores capable of containing the RTD. (b) Photo of a sealed cell mounted on a (blue) magnetic stirrer. The upper parts of the RTD are visible, as is the gas injection line which is terminated at a valve and contains the pressure transducer. The cell is surrounded by six Peltier elements, each compressed between the cell and a coolant block. (For interpretation of the references to color in this figure legend, the reader is referred to the web version of this article.)

5.5 K·min⁻¹. Faster temperature ramping is achievable, but in such cases the ramp rate will not necessarily be constant over the entire temperature range.

A cross-shaped PTFE stirring flea (approximate volume of 0.8 cm³) is used to apply shear to the fluid in each cell. The flea is driven at 700 rpm using a magnetic stirrer (color squid; IKA Works, Inc.) on which the cell sits in a central location. Data acquisition and instrument control are achieved *via* a National Instruments CompactDAQ system used with a data acquisition rate of 1 Hz. During the entire experiment, the cell temperature and gas phase pressure are continuously monitored. Finally, we note that as a safety precaution to avoid overheating the cells, thermal switches on the cell lids will shut off the power supplies driving the Peltier elements if the cell temperature exceeds a critical value.

Thermal lags and spatial gradients within the stirred fluid volume during cooling (see Fig. 4) were modelled using two dimensional CFD (computational fluid dynamics) simulations performed with ANSYS FLUENT (finite-volume based). The "Coupled Method" in FLUENT was
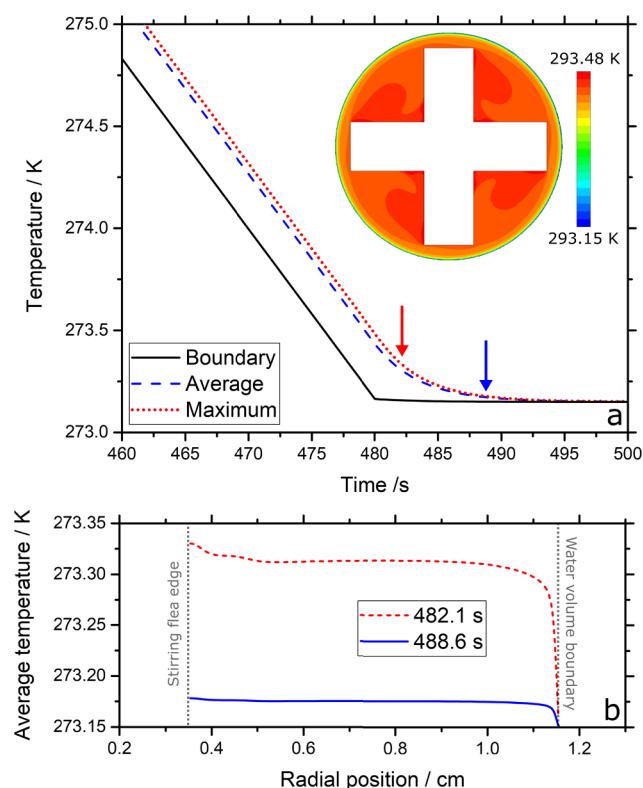
Fig. 4. Results from CFD simulations. (a) Maximum and spatially averaged water temperatures versus time together with the temperature of the cooled water at the boundary of the cell. We focus on the end of a cooling ramp where the ramp rate was $5\,\mathrm{K\cdot min^{-1}}$. Inset shows a snapshot of the CFD simulation system at time = 240 s with a color map of the water temperature. The rotation direction for the flea is counter clockwise. The flea is 20 mm long with arm widths of 5 mm. The well diameter is 23.1 mm. (b) Spatially-resolved water temperature across half of the cell near the end of the cooling ramp (482.1 s; red arrow in (a)) and toward the end of the thermalisation period (488.6 s; blue arrow in (a)). (For interpretation of the references to color in this figure legend, the reader is referred to the web version of this article.)

used for pressure-velocity coupling with spatial discretization for the momentum, turbulence and heat equations implemented *via* the 3rd order MUSCL scheme [25,26]. Spatial discretization of the pressure field was performed *via* the 2nd order method, with time stepping resolved using an implicit bounded 2nd order method. As the cell does not contain baffles, the flow was treated using a single domain with the rotation of the flea handled using the moving reference frame method. This also allowed the use of a steady-state method to initialize the system to the required temperature. The RNG k-epsilon turbulence model [27] with the Kato-Launder Production Limiter [28] was selected as it has the best balance between accuracy and performance in rotating flows. The viscous heating term (e.g. [29]) was included to capture the heating caused by the dissipation of the turbulence energy. To simulate a cooling ramp, the boundary conditions were chosen such that the temperature at edge of the water volume decreased linearly with time until the set point was reached.

The results of the CFD simulations are presented in Fig. 4: during a $5\,\mathrm{K\cdot min^{-1}}$ cooling ramp, the thermal lag causes an approximately 0.3 K higher average water temperature compared to the boundary temperature. As seen in the inset of Fig. 4a, and also in Fig. 4b, the highest spatial temperature gradient is in the vicinity of the wall (approximately $0.8\,\mathrm{K\cdot mm^{-1}}$ near the end of the cooling ramp at 482.1 s). However, upon reaching the target temperature, the stirring causes the water volume to obtain thermal equilibrium over a time scale of approximately 10 s (Fig. 4a). This time scale is more than an order of magnitude smaller than the shortest mean induction time measured in

this work, which indicates that thermal lags across the water volume are of limited significance. The simulation results also suggest that the temperature rise due to the stirrer is negligible at 700 rpm: the maximum temperature change due to viscous heating of the water is approximately 0.3 mK.

2.2. Experimental protocol

The sII hydrate forming gas mixture used in these experiments had the following composition $0.9039CH_4 + 0.0571C_2H_6 + 0.019C_3H_8 + 0.02CO_2$ where fractions are on a molar basis. This mixture was also used for the experiments detailed by May et al. [7]. Prior to starting any experiments, the cell was first cleaned using the following solvent sequence: toluene, ethanol, isopropanol. Following a rinse with deionised water, the cell was dried and then filled with 5 mL of deionized water which had been degassed under vacuum. The degassing of the water was carried out for at least 30 min with agitation using a separate heated plate set to approximately 75 °C. Following liquid loading, the cell was sealed and purged three times with the hydrate-forming gas mixture. The system was then initialized with that mixture to a pressure of 13 MPa at a temperature of 22 °C while applying shear to the system at 700 rpm to ensure effective dissolution of gas into the water. The cell was subsequently isolated and operated isochorically.

The cell temperature was repeatedly cycled into and out of the hydrate equilibrium region. The boundary of the hydrate region, the hydrate dissociation curve, was predicted using the Cubic Plus Association (CPA) model in Multiflash [30] (see Fig. 1). Each cycle started with a 5 min isothermal period at a regeneration temperature, $T_{regen} = 40$ °C, under (the same) constant shear. When applied between successive measurements of hydrate formation, this regeneration period ensures complete dissociation of any hydrates produced during the previous cooling ramp. No evidence of the so-called memory effect [14] was observed. The cell temperature was then decreased at ramp rate, β, to a target temperature at which the cell conditions were within the hydrate stability region. The target temperature was chosen to be sufficiently high to avoid formation during the cooling ramp and thus yield well-defined pressure-time plateaus. This helps to ensure that the automatic analysis method (detailed below) is successful and accurate. After cooling at $(3–6)\,\mathrm{K\cdot min^{-1}}$, the system remained at the target temperature until hydrate formation was unambiguously detected. This was achieved by monitoring the cell pressure, with automated detection of hydrate formation being triggered by a drop of at least 0.4 MPa with respect to the cell pressure at the end of the cooling ramp. Once hydrate formation was detected, the system temperature was returned to T_{regen} and the cycle repeated. Unlike other studies, a maximum induction time limit was not set. This is especially critical at lower subcoolings where (e.g.) the experimental time limit of 15,000 s imposed by Wu et al. [13] can lead to an artificial truncation of the induction time distributions. While Adamova et al. [31] have recently developed a method of estimating nucleation rates from data sets that sub-sample the induction time distribution, there is still a requirement to obtain a sufficient number of induction time data to obtain a reliable estimate. Moreover, a comprehensive sampling of the full distribution allows the application of statistical tests to determine the nature of that distribution (e.g. for exponentially distributed values, the mean and standard deviation should be the same).

Fig. 5a and b show example experimental temperature- and pressure-time traces, respectively. The latter is separated into the three phases outlined above: the cooling-induced pressure decrease, the isothermal induction time period and the hydrate growth phase which follows the onset of detectable hydrate formation. The 0.4 MPa drop is used by the control algorithm implemented in the data acquisition software to determine when the cell should be regenerated. However, it is not used to extract the induction time since the time from the ramp start to the generation of the pressure drop includes a finite period of
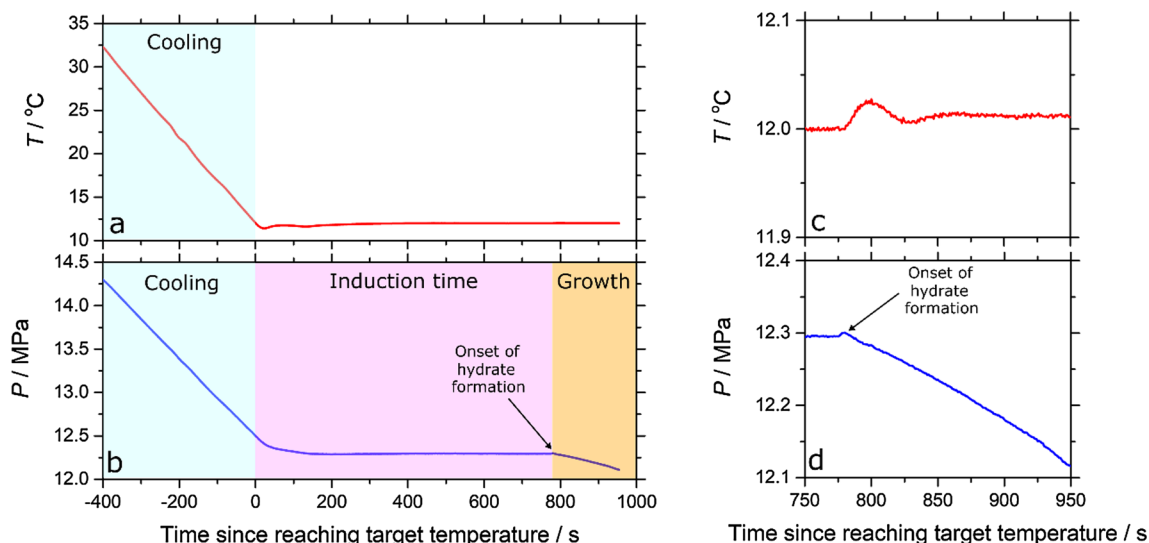
Fig. 5. Temperature (a) and pressure (b) during an induction time experiment at a target temperature of 12 °C (ΔT = 7.9 K). Temperature and pressure time series data at the onset of gas consumption are shown in (c,d). Small, coincident pressure and temperature increases are seen at this point.

growth following the onset of formation. Instead, as for the constant cooling experiments detailed by [7], the pressure and temperature time series data are post-processed to determine the onset of detectable hydrate formation using an analysis method detailed in the following section.

Often, at the point of gas consumption onset, a small and very brief *increase* in the gas pressure was observed (Fig. 5d), coincident with a small and brief temperature increase registered by the cell RTD (Fig. 5c). Since all formation events in this work occur above the ice point, these signals can be attributed to the exothermic formation of a discrete amount of hydrate (recalescence; e.g. [32]). Such observations are consistent with the occurrence of a discrete nucleation event after a relatively long induction time, rather than the alternative: the slow growth of unresolved amounts of hydrate for a significant period of time before the detection threshold is reached would not lead to the observed transient increases in temperature and pressure.

Finally, as illustrated by the data shown in Fig. 5b, the growth-induced pressure decrease that follows formation is relatively constant and readily measured. The average rate of this pressure decrease is determined over the first 0.05 MPa following formation and is then used to determine the dependence of the initial hydrate growth rate on subcooling. To estimate a gas consumption rate, the measured average rate of pressure decrease is simply multiplied by V/ZRT, where V is the gas phase volume (5.1 mL), Z is the compressibility factor estimated from the CPA EOS (≈ 0.8), and R is the ideal gas constant.

2.3. Automated detection of hydrate formation

The induction time, t_i, for hydrate formation at constant subcooling is defined here as the time between the system first reaching the target temperature and the time of hydrate formation onset (t_f). The detection algorithm used to determine t_i for each formation-regeneration cycle commences by making an initial *estimate* of the formation time (onset of a reduction in the gas pressure) which we denote $t_{f,est}$. The end of the formation-regeneration cycle corresponds to the moment when a pressure drop of 0.4 MPa is measured which is followed by the re-heating of the cell. The algorithm searches through the pressure-time dataset measured for this cycle by stepping back from the end of the data set, which is concurrently smoothed via a 21-point-wide moving window average, until the difference in pressure between consecutive time steps is no longer positive: this occurs upon reaching the approximate end of the isobaric pressure-time plateau. An example of the result of such an analysis is shown in Fig. 6. The smoothing minimises
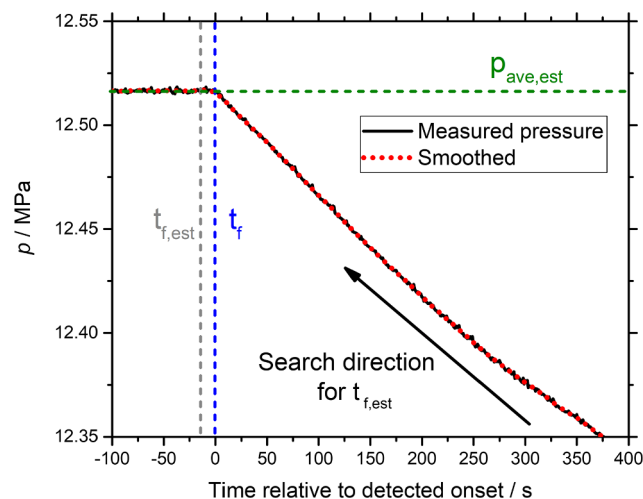

Fig. 6. Example for a subcooling of $\Delta T = 6$ K demonstrating the automated search for the formation time, t_f. To do so an initial estimate of the formation time, $t_{f,est}$, is found from the smoothed pressure-time data where the pressure stops increasing in the search direction. An average pressure, $p_{ave,est}$, for the plateau 60 s before $t_{f,est}$ is then calculated to identify the formation time accurately.

unwanted effects from (the low) signal noise in the pressure transducer. The smoothed dataset is calculated sequentially for each point while stepping back through the pressure-time series data meaning that only points between $t_{f,est}$ and the end of the dataset are smoothed. The data smoothing results in a value of $t_{f,est}$ that usually occurs slightly earlier than the actual formation time (as in Fig. 6). For cycles with long induction times, the algorithm has the advantage of avoiding the need to process the entire dataset because it commences the search from the end of the cycle.

To find a more accurate measurement of the formation time, the average system pressure for 1 min prior to $t_{f,est}$ is calculated to yield $p_{ave,est}$, as shown in Fig. 6 (the average pressure is evaluated using the smoothed pressure signal during that minute). The formation time, t_f, is then identified as the time, $t > t_{f,est}$, for which the pressure passes below $p_{ave,est}$ *and* stays below $p_{ave,est}$ until the end of the dataset (i.e. $p < p_{ave,est}$ for $t > t_f$).

This approach works well for data such as those shown in Fig. 6; however, for the particular dataset in Fig. 5, the algorithm identifies the

formation time as occurring just after the pressure peak. This corresponds to an error of about 10 s relative to the start of the pressure peak, where hydrate formation is inferred from the exothermic response. Such an error is usually negligible compared to the overall induction time, and in cases where it is not (e.g. induction times less than 1 min) a slightly modified algorithm suited to short plateaus is used. As a check of the results obtained by the automated detection method, plots such as that shown in Fig. 6 are always automatically generated to allow for rapid, visual validation of the algorithm.

May et al. [7,14] constructed cumulative formation probability distributions as a function of subcooling from their ramped-temperature, constant cooling experiments. Analogously, the induction times measured here were binned and then numerically integrated to yield a cumulative probability distribution for hydrate formation versus induction time. However, because the induction times are exponentially distributed, we use bin widths which increase logarithmically in time (20 bins per decade of induction time). This enables resolution of the fast initial growth of the exponential distribution while avoiding isolated, unphysical plateaus in the cumulative probability at longer induction times due to a combination of rare, long induction time events with a constant, small bin width.

Histograms of the initial growth rate measured following t_f in each formation-regeneration cycle were also constructed; here a constant bin width equivalent to a pressure reduction rate of 10^{-4} MPa·s^{-1} was used. May et al. [7] estimated the minimum amount of hydrate formation resolvable by the measurement of a statistically significant pressure drop (0.005 MPa) in a comparable gas volume (3.5 mL) to be about 1 μmol or 20 μg. The amount of hydrate growth corresponding to the 0.4 MPa drop measured in each formation-regeneration cycle is 80 μmol or 1.6 mg, which is sufficiently small relative to the system size (5 g of water and 0.3 g of gas) that no suppression of the growth rate is likely to have occurred due to heat or mass transfer limitations.

3. Results and discussion

3.1. Induction time distributions

Four induction time probability distributions with between 83 and 312 hydrate formation events were measured at subcoolings of (6.0, 6.9, 7.9 and 9.7) K. Table 1 shows the mean induction times and standard deviations for each distribution together with the maximum and minimum induction times and the number of measurements at each particular subcooling. Increasing the driving force for hydrate formation *via* an increase in the subcooling leads to decreased induction times. The mean and standard deviations match closely, a characteristic of exponentially distributed values (e.g. [33]). This is a first indication of the data's consistency with the predictions of Eq. (1). The cumulative probability distribution functions (CPDFs) for the induction time at the four subcooling values are shown in Fig. 7. Fits to the data with Eq. (1) (solid curves in Fig. 7), using J as the only adjustable parameter, indicate that the functional form suggested by the mononuclear nucleation mechanism in CNT applies well to the data obtained here, with no need to include a lag time parameter.
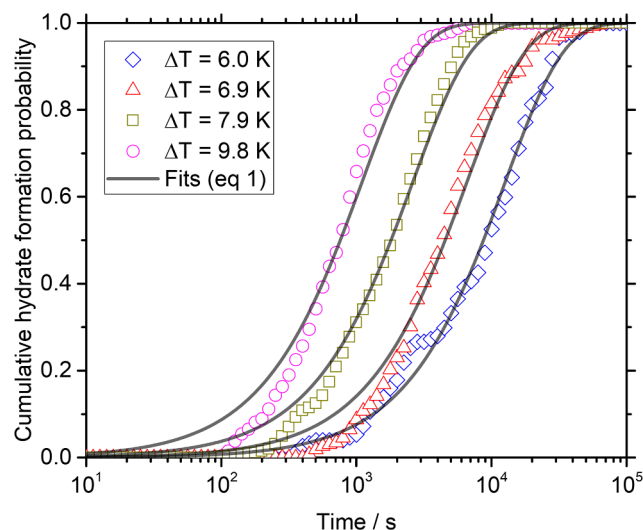

Fig. 7. Cumulative probability of hydrate formation versus time for four subcooling values. Grey transparent lines are fits of Eq. (1) to the data, with J being the only adjustable parameter.
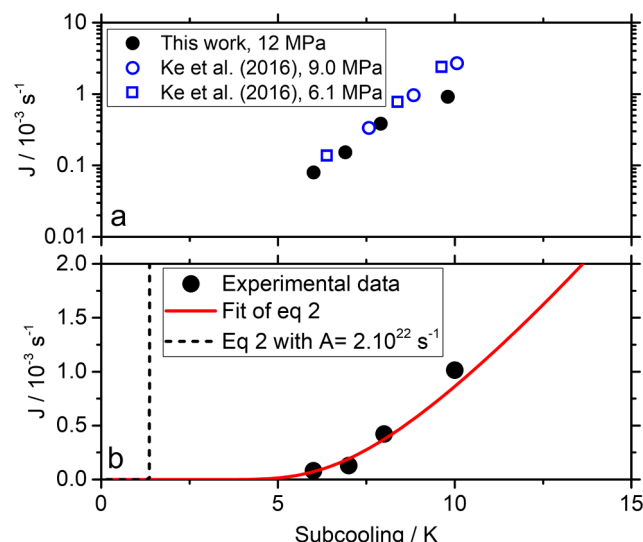

Fig. 8. (a) Nucleation rate, J, versus subcooling as extracted from fits of Eq. (1) to the cumulative hydrate formation probability distributions in Fig. 7, together with nucleation rates measured independently by Ke *et al.* [23]. (b) Nucleation rate as a function of subcooling including both a fit of Eq. (2) to the measured data (red solid line) together with a plot of Eq. (2) using a value of $A = 2 \times 10^{22}$ s^{-1} based on predictions from Classical Nucleation Theory [15] (dashed line). The latter was plotted assuming a nucleation area of 20 cm^2 which is approximately that of the wetted area of the interior of the cell.

Table 1
Statistics of the induction time (t_i) distributions measured at each subcooling value, ΔT (mean t_i, standard deviation, maximum t_i, minimum t_i and number of measured formation events, N) together with the extracted nucleation rate, J. Values of the pressure, p, and absolute temperature, T, at which the formation was measured are also listed. To facilitate comparison with other laboratory measurements where only normalized nucleation rates are given, we also give rates normalized to the wetted area of the cell's steel internal surfaces, A_{wetted} (approximately 20 cm^2), which is the interface where nucleation is most likely to occur in a well-stirred system. However, making assumptions about which interface in a given system is responsible for nucleation can be problematic (see text).

ΔT/K	Mean t_i /s	Std dev./s	Max t_i/s	Min t_i/s	N	$10^4 J/s^{-1}$	$(J/A_{wetted})/m^{-2}\cdot s^{-1}$	T/K	p/MPa
6.0	11,249	9.858	45,382	326	75	0.80 ± 0.09	0.040 ± 0.005	14.0	12.5
6.9	6596	8447	57,754	422	130	1.53 ± 0.02	0.077 ± 0.001	13.0	12.3
7.9	2203	1882	10,873	97	300	3.85 ± 0.06	0.193 ± 0.003	12.0	12.3
9.8	947	968	5874	26	131	9.15 ± 0.19	0.458 ± 0.010	10.0	12.1

Fitting Eq. (1) to the data in Fig. 7 enables an extraction of J as a function of ΔT, the results of which are plotted in Fig. 8. The extracted nucleation rate increases with subcooling, varying from $8.0 \times 10^{-5}\,s^{-1}$ at 6 K to $9.2 \times 10^{-4}\,s^{-1}$ at 9.8 K. In Fig. 8a we also show a comparison of the nucleation rates determined in this work with those measured independently by Ke et al. [23] via induction time measurements using a titanium autoclave for sII hydrates at comparable pressures. Considering the stochasticity of hydrate formation and the challenges normally associated with reproducible experimental characterisation, the consistency between these two independent data sets (within a factor of three or better) suggests that the nucleation rates being measured may have some broader generality.

Nucleation rates depend on either system volume for homogenous nucleation in the bulk (rarely observed in practice) or on the size of the interfacial area where heterogenous nucleation occurs. Identifying which interfacial area is responsible for the nucleation is difficult and this often presents a barrier to meaningful comparisons between nucleation rates measured in different experiments. In Table 1, we also list nucleation rates normalised by the wetted area of the cells' steel internal surfaces, A_{wetted}, which is the interface suggested by theory to be most likely responsible for nucleation in a well-stirred system [15]. This said, any such choice of interface can be problematic because it is often non-trivial to determine (i) which interface is actually relevant; and (ii) if nucleation is occurring on a finite number of sites (e.g. corresponding to major surface imperfections), the number of which may not necessarily scale in proportion to the area of the selected interface. The quiescent experiments of Maeda [34,35], where quasi-free water droplets were suspended in perfluorodecalin and squalane without contacting a solid surface, are notable exceptions in that there was only one type of interface with known area available for nucleation. The interface was between two liquids and the driving force for nucleation was contingent upon the solubility of methane and propane within the non-aqueous liquid.

One objective of this work is to encourage quantitative comparisons between different measurements of nucleation rates without undue reliance on assumptions about the interfaces responsible. This can be achieved by interpreting the absolute nucleation rates (i.e. those plotted Fig. 8a) observed in different experiments using a framework based on Classical Nucleation Theory. As shown below, such an approach reveals an unexpected but noteworthy similarity (factor on the order of 10) in absolute nucleation rates measured in several experiments with different apparatus, despite their different sizes and without definitive information from the experiments about which interface was responsible for the nucleation.

3.2. Comparisons with Classical nucleation theory

Kashchiev and Firoozabadi used CNT to make predictions specific to gas hydrate nucleation for the subcooling-dependence of J [15]. Their model for the nucleation rate, which defines the rate of appearance of critically-sized hydrate nuclei and is dependent on both absolute temperature and subcooling, can be written in terms of a kinetic parameter, A, and a thermodynamic parameter, B' as follows:

$$J(\Delta T,\, T) = A \exp\left(\frac{\Delta s_e \Delta T}{k_B T}\right) \exp\left(-\frac{B'}{T \Delta T^2}\right) \tag{2}$$

Here Δs_e is the entropy of hydrate dissociation per hydrate building unit at T_e and k_B is the Boltzmann constant: for an isobaric process the driving force for hydrate formation is given by $\Delta\mu \approx \Delta s_e \Delta T$ [15]. For the hydrate-water-gas equilibrium at 12 MPa, as considered in this work, the enthalpy of hydrate dissociation was calculated to be $\Delta s_e = 20\,k_B$ using the CPA EOS in Multiflash 6.2 [30]. Using this value of Δs_e, the experimentally observed subcooling-dependence of J, as extracted above from the induction time measurements, is regressed to Eq. (2) by treating A and B' as adjustable parameters. As discussed by

May et al. [7], the orthogonality of these parameters is reasonable and good fits of the data are achieved (red line in Fig. 8b). This enables the extraction of $A = (2.1 \pm 0.4) \times 10^{-3}\,s^{-1}$ and $B' = (4.1 \pm 0.5) \times 10^4\,K^3$, where the error bounds denote the statistical uncertainty of the fit. Similar values of A and B' are extracted by regression of the nucleation rates measured by Ke et al. [23].

The value of B' measured in this work is consistent within the statistical uncertainty with values obtained for the same gas mixture *via* constant cooling measurements (constant temperature ramping) using the 1st generation apparatus (HPS-ALTA-1) [7]. However, the kinetic parameter, A, as measured using the HPS-ALTA-1 via constant cooling experiments is about a factor of 10 larger than the value obtained here. This difference is likely due in part to the dynamic effects inherent in ramped temperature experiments. For example, Kulkarni et al. demonstrated that fitted values of A obtained from measurements of crystal nucleation via ramped temperature experiments exhibit a clear dependence on cooling rate [19]. Fortunately, given the degree of orthogonality between B' and A, consistent values of the nucleation work (parametrized by B') are obtainable by regression to datasets from both isothermal and ramped temperature experiments, even when the corresponding A values vary by an order of magnitude.

Experimental values of A and B' can be compared directly with values expected from the theory underlying Eq. (2). According to the CNT-based model, the kinetic parameter, $A = z f N_0$, is dependent on the attachment frequency, f, of hydrate building units to the hydrate nucleus, the number of nucleation sites, N_0, and the Zeldovich factor, $z \approx 0.01$ to 1. Often, N_0 is written as the product of the areal density of nucleation sites and the interfacial area where heterogenous nucleation occurs on the assumption that the nucleation sites are distributed uniformly across that interface. The thermodynamic parameter or nucleation work is parameterized by $B' = \frac{4c^3 v_h^2 \sigma_{ef}^3}{27 k_B \Delta s_e^2}$, where c is a geometric shape factor for the critical nucleus (equal to $(36\pi)^{1/3}$ for spherical, cap or lens-shaped hydrate clusters, the latter two relevant for nucleation on solid interfaces), and v_h is the volume of a hydrate building unit containing one gas molecule and n_w water molecules ($0.647\,nm^3$ with $n_w = 5.67$ for sII hydrates). Kashchiev and Firoozabadi [15] took the free energy of the hydrate-water interface for homogenous nucleation as $\sigma_{ef} = 20\,mJ \cdot m^{-2}$, based upon estimates of the surface free energy of water-ice interfaces. For the (more likely observed) case of heterogeneous nucleation (HEN), this value is reduced by the cosine of the contact angle at the steel-hydrate-water interface [15]. The measured value of B' is consistent with the theoretical prediction of its value if the contact angle is approximately 15°.

While our preference is to avoid making assumptions about the interface responsible, the nucleation observed in this work could have potentially occurred on the PTFE-coated stirrer instead of the wetted steel walls. However, the latter interface is considered the more likely of the two for the following reasons: (a) it is plausible that the wetting angle of the hydrate on hydrophilic steel is smaller than the wetting angle of the hydrate on hydrophobic PTFE and (b) Tanaka et al. [36] found that hydrates preferentially nucleated on the water-gas interface rather than the water-gas-PTFE three phase line or the PTFE-water interface. This observation is also consistent with results from other studies of hydrate nucleation [12] and ice nucleation (e.g. [37]) in which reduced nucleation rates were observed as the hydrophobicity of the surface supporting or containing the water phase was increased.

The value of B' determined in this work can be used with another result from CNT to estimate the number of building units, n^*, required to form a critical hydrate nucleus [15]:

$$n^* = 2k_B B'/\Delta s_e \Delta T^3 \tag{3}$$

Application of Eq. (3) using the value of B' determined in this work results in values of n^* ranging from about 18 at $\Delta T = 6$ K to 4 at $\Delta T = 10$ K. While a precise definition of the building unit involved in hydrate nucleation remains outstanding, this result demonstrates the

potential power of applying the CNT-based model to the interpretation of robust hydrate nucleation measurements, particularly in terms of the thermodynamic barrier to nucleation.

While the agreement between experiment and the CNT-based model is promising for the description of nucleation work, the inconsistency between the measured and theoretical values of A is extreme, at least upon first consideration. The CNT-based model [15] predicts that the areal concentration of nucleation sites is on the order of 10^{21} cm^{-2}.s^{-1} (for reference, the bulk concentration of sites for homogeneous nucleation is estimated to be 10^{29} cm^{-3}.s^{-1}). Multiplying this value by the wetted area (approximately 20 cm^2) of the internal steel surfaces of the HPS-ALTA-2 (the interface where the hydrate nucleation work is lowest [15]) and inserting it into Eq. (2) yields a predicted nucleation rate that is shown by the dotted line in Fig. 8b. One sees that with increasing subcooling, this predicted nucleation rate grows orders of magnitude faster than that observed in our experiments or in those of Ke et al [23] (even if the increased dimensions of the autoclaves used in reference [23] are taken into consideration). The impact of such large values of A on the nucleation rate would be to make hydrate nucleation effectively indistinguishable from a deterministic process at subcoolings around 2 K.

Kashchiev and Firoozabadi [15] used their model to fit the experimental data reported by Makogon [38] for methane (sI) hydrate nucleation. Hydrates were observed in those experiments on the water-gas interface but, as proposed by Maeda [34,39], in such cases hydrates will likely nucleate on the steel surface in contact with that interface. Kashchiev and Firoozabadi [15] obtained a value of $B' = (1.59 \pm 0.14) \times 10^4$ K^3 consistent with theory (assuming a 20° wetting angle on the steel), in excellent agreement with the value obtained by May et al. [7] for pure CH$_4$ hydrates (2.1×10^4 K^3), and within a factor of 2.6 with the value obtained here for the gas mixture. However, the area-normalised HEN kinetic parameter Kashchiev and Firoozabadi obtained from analysing Makogon's experimental data was 1.56×10^{-3} cm^{-2}.s^{-1}, some 24 orders of magnitude smaller than the prediction elaborated on in most of their paper. They reconciled this discrepancy by concluding that the observed nucleation rates were the result of HEN occurring on a very small number of sites with low nucleation work. In contrast, the theoretical value of A assumes the number of nucleation sites is of order 10^{14} cm^{-2}, based on the cross sectional area of a water molecule.

The value of A obtained from the data in Table 1 corresponds to an area-normalised kinetic parameter for HEN of 0.11×10^{-3} cm^{-2}.s^{-1} based on the wetted area of the cell's steel internal surfaces. This is within a factor of 14 of the value obtained from the data of Makogon [38] by Kashchiev and Firoozabadi [15]; however such a comparison relies on assumptions about the interfaces responsible for nucleation in both cases. Kashchiev and Firoozabadi [15] excluded the data point measured at the lowest subcooling by Makogon [38] from their analysis: if it is included the agreement with the result obtained in this work improves to within a factor of 7.

Maeda [40] used constant cooling ramps to measure nucleation rates for sII methane-propane gas hydrates in the presence of a stainless steel wall using a quiescent apparatus. While some clear differences exist between that experiment and the one described in the present work (quiescent vs stirred, constant cooling vs isothermal, cell diameter of 5 mm vs 24 mm), it is instructive to compare the observed nucleation rates, particularly in the context of the very large differences observed with nucleation rates estimated from theory or simulation. From Fig. 4 of Maeda [40], the normalised nucleation rates at about 8 K and 10 K are approximately 0.001 m^{-1}·s^{-1} and 0.002 m^{-1}·s^{-1}, respectively, with the normalisation length scale specified as the circumference of a 5 mm diameter circle. Reconstructing the observed nucleation rates gives 2×10^{-5} s^{-1} at 8 K subcooling and 3×10^{-5} s^{-1} at 10 K. In the present work we observed (Table 1) nucleation rates of 38.5×10^{-5} s^{-1} at 7.9 K subcooling and 91.5×10^{-5} s^{-1} at 9.8 K, which are between 20 and 30 times larger. These differences are still

small compared to those found with theoretical predictions, and likely explained by the aforementioned differences between the experiments (particularly quiescent vs stirred). If the nucleation rates listed in Table 1 are normalised relative to the circumference of the HPS-ALTA gas-water-steel interfacial line, the agreement with the data of Maeda et al. [40] improves to within a factor of 5–6.

The experimental comparisons of nucleation rate considered here suggest three key results. First, several different measurements of gas hydrate nucleation rate at industrially-accessible sub-cooling conditions are consistent within a factor of 30, independent of the interface selected (if one is chosen at all). This is noteworthy given the significant differences in experiment size, level of shear, and method of setting the driving force. For two experiments in well-sheared systems at constant subcooling the consistency was within a factor of three. Second, the CNT framework of Kashchiev and Firoozabadi [15] does a reasonable job describing these experimental data sets in terms of the model's functional form and the thermodynamic parameter (nucleation work). Third, the kinetic parameter A is not currently representative of macroscopic systems with the theoretical values derived by Kashchiev & Firoozabadi [15] differing by many (> 20) orders of magnitude from the values needed to explain the comparatively consistent experimental observations.

The problem with the CNT framework relating to A should not be the basis of dismissing the model, given the successes it has describing the data mentioned in point 2. Rather, we propose that consistent experimental results be used to constrain and improve theoretical estimates of the constituent factors that determine A. For example, if the number of low nucleation work sites in the HPS-ALTA-2 cell is set to the minimum possible value, i.e. $N_0 = 1$, then the attachment frequency of the hydrate building units to the nucleus is (0.002 to 0.2) Hz. This is very different to the 0.5 GHz estimated from CNT by Kashchiev and Firoozabadi [15]. Given that the number of low nucleation work sites within the HPS-ALTA-2 cell is likely to be larger than 1, the attachment frequency of hydrate building units is probably smaller than 10^{-3} Hz at the low subcoolings (< 10 K) accessed in these experiments.

This analysis also suggests future experiments in which the number of nucleation sites available within a given system is varied by adding a quantified amount of a seeding agent. Sowa et al. [41] investigated the use of AgI to promote hydrate nucleation using a quiescent HP-ALTA apparatus. Although (i) AgI is a known promoter of ice nucleation, (ii) ice is a known promoter of hydrate nucleation, and (iii) the average hydrate formation temperatures achieved in the quiescent HP-ALTA experiments of Sowa et al. [41] were well below 0 °C, no significant effect on the hydrate formation probability distribution was observed with AgI relative to the baseline experiments. However, this might reflect the direct nucleation of hydrate without ice forming first on the AgI. Alternatively, the extent of nucleation promotion by the AgI-ice mechanism may have been small in comparison with the contribution due to sites with low nucleation work on the apparatus walls responsible for the baseline nucleation rate. Further studies investigating the effect of AgI or other prospective nucleation promoters on hydrate formation are warranted but they should consider these factors as part of their experimental design.

3.3. Hydrate growth rates

The subcooling dependence of the hydrate growth rate immediately following formation was quantified by the rate of gas consumption. As can be seen in Fig. 9a–d, the hydrate growth rates observed were a stochastic quantity with a mean that increased with subcooling. This stochasticity is likely to arise due to run-to-run variations in the nature of the growing hydrate phase. We speculate that these variations are linked not only to the stochasticity of the nucleation event itself but also to variations in gas composition within the water during growth.

Based on isothermal growth rate data from Bishnoi and co-workers [42–44], Turner et al. [45] proposed that the gas consumption rate, G,
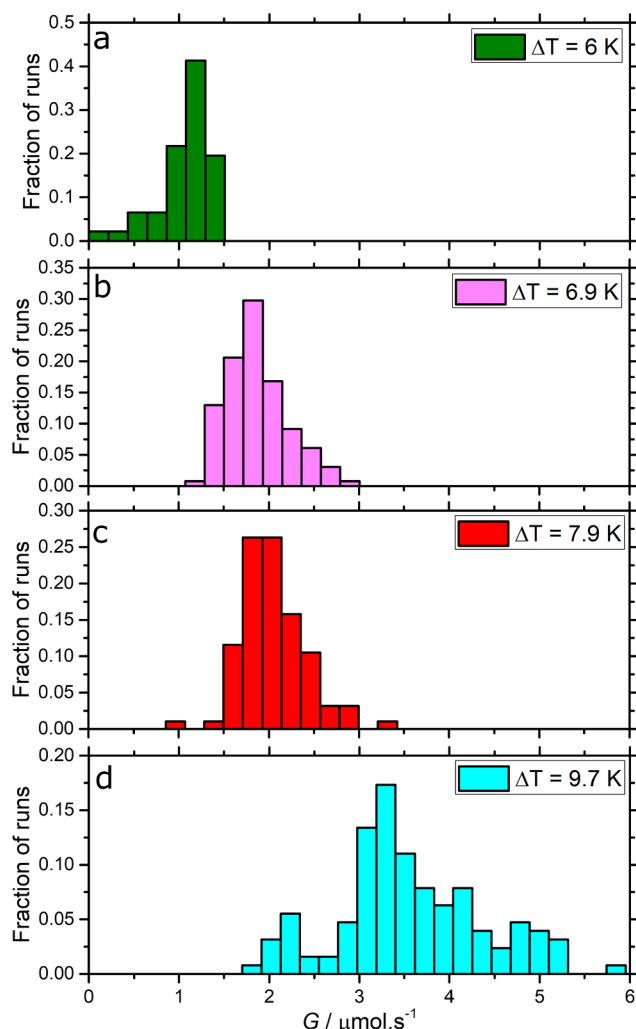
Fig. 9. Probability densities for initial hydrate growth rates for subcooling values of (a) 6 K, (b) 6.9 K, (c) 7.9 K and (d) 9.7 K.

is proportional to the product of the gas-water interfacial area, a, and the subcooling:

$$G = -\frac{dn}{dt} \propto a\Delta T \tag{4}$$

where n is the amount of gas present. In Fig. 10 we plot the mean gas consumption rate versus subcooling and observe a trend which, to a
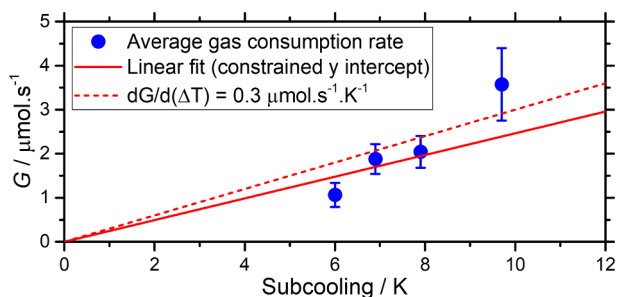

Fig. 10. Mean growth rate plotted versus subcooling (error bars correspond to the standard deviations of the measured growth rates). The solid red line is a linear fit to the data where we have constrained G to be zero at zero subcooling. The dashed line is the G-ΔT relationship expected from the growth rate determined from the data of Englezos et al. for a methane-ethane mixture [42]. (For interpretation of the references to color in this figure legend, the reader is referred to the web version of this article.)

first approximation, is consistent with a linear dependence of G on ΔT. From a linear fit to the data where G is constrained as zero at $\Delta T = 0$, we extract a growth rate per unit subcooling of $dG/d(\Delta T) = (0.25 \pm 0.03)$ µmol.s^{-1}.K^{-1}. Analogous to the analysis carried out by Turner et al. [45], we have revisited the data of Englezos *et al* for a 75.02% methane / 24.98% ethane mixture [42] from which we have estimated an areal growth rate value per unit subcooling of 0.03 µmol.s^{-1}.K^{-1}.cm^{-2}. Combining this latter value with an estimate of the gas–water interfacial area in the HPS-ALTA-2 (10 cm^2) yields a value of $dG/d(\Delta T) = 0.3$ µmol.s^{-1}.K^{-1}, which is within 20% of our measured value.

4. Conclusion

A second generation, high pressure, stirred ALTA (HPS-ALTA-2) was developed and used to measure hydrate formation probability distributions at a fixed subcooling which contain statistically significant numbers of induction time measurements. The upgraded HPS-ALTA cell is equipped with six thermoelectric Peltier elements which enable rapid, radially symmetric heating and cooling of the cell, with minimal lags or gradients. The induction times measured for a synthetic natural gas mixture at subcoolings ranging from 6.0 K to 9.8 K were exponentially distributed and consistent with the mononucleation mechanism from Classical Nucleation Theory. The nucleation rates measured at each subcooling were consistent within a factor of three with values measured in independent laboratories using much larger autoclaves.

Hydrate growth rates, as measured by rates of gas consumption for a brief period after nucleation, were also measured and observed to be stochastic with mean values that increased approximately linearly with subcooling. The slope of the fitted data agreed well with that found previously for a methane-ethane gas mixture. These results establish that, while stochastic, nucleation and growth phenomena in natural gas hydrates can be reproducibly measured and compared quantitatively in a meaningful way with a clear prospect of generalised interpretation.

Central to such a generalised interpretation is the theoretical framework based on CNT developed for application to gas hydrates by Kashchiev and Firoozabadi [15]. Many aspects of the measured induction time distributions and nucleation rates are consistent with the predictions of this model, particularly for the nucleation work associated with critical nucleus formation. However, the discrepancy between the measured and predicted kinetic nucleation parameters have two implications for the CNT model framework: (i) the observed heterogeneous nucleation rates are due to the presence of a small number of sites with low nucleation work, and (ii) the attachment frequency of hydrate building units is much smaller than current CNT estimates.

Future work should attempt to reconcile this discrepancy between the measured and predicted attachment frequency, potentially through an improved definition of the nature of a 'hydrate building unit'. While central to the framework of CNT and clearly applicable to the description of nuclei formed from a pure substance, building units or monomers are incongruent with the multi-component nature of hydrates as well as their microscopic clathrate structure. Potentially this is an area where molecular dynamic simulations are applicable to augment robust experimental studies with the objective of extending the CNT framework sufficiently to provide engineering models of hydrate formation.

contributions to the apparatus development, Bruce Norris and Thomas Charlton for useful discussions regarding hydrate growth rates and Andrew Pelc for analysis of hydrate growth rate data from the literature.

References

[1] Sloan, E.D. and C.A. Koh, Clathrate Hydrates of Natural Gases, Third Edition. Clathrate Hydrates of Natural Gases, Third Edition, 2008. 119: p. 1-701.

[2] May EF, Marsh KN, Goodwin ARH. Frontier oil and gas: deep-water and the arctic. Second Ed. Future Energy: Improved, Sustainable and Clean Options for our Planet; 2014. p. 75–93.

[3] Cochrane S. Hydrate control and remediation best practices in deepwater oil environments. Houston, Texas, USA: Offshore Technology Conference; 2003.

[4] Sloan ED. A changing hydrate paradigm – from apprehension to avoidance to risk management. Fluid Phase Equilib 2005;228:67–74.

[5] Ke W, Kelland MA. Kinetic hydrate inhibitor studies for gas hydrate systems: a review of experimental equipment and test methods. Energy Fuels 2016;30(12):10015–28.

[6] Ke W, Svartaas TM, Chen D. A review of gas hydrate nucleation theories and growth models. J Nat Gas Sci Eng 2019;61:169–96.

[7] May EF, et al. Gas hydrate formation probability distributions: the effect of shear & comparisons with nucleation theory. Langmuir 2018;34:3186.

[8] Abay HK, Svartaas TM. Effect of ultralow concentration of methanol on methane hydrate formation. Energy Fuels 2010;24:752–7.

[9] Lone A, Kelland MA. Exploring kinetic hydrate inhibitor test methods and conditions using a multicell steel rocker rig. Energy Fuels 2013;27(5):2536–47.

[10] Barlow TW, Haymet ADJ. Alta – an Automated Lag-Time apparatus for studying the nucleation of supercooled liquids. Rev Sci Instrum 1995;66(4):2996–3007.

[11] Wilson PW, Lester D, Haymet ADJ. Heterogeneous nucleation of clathrates from supercooled tetrahydrofuran (THF)/water mixtures, and the effect of an added catalyst. Chem Eng Sci 2005;60(11):2937–41.

[12] Maeda N. Measurements of gas hydrate formation probability distributions on a quasi-free water droplet. Rev Sci Instrum 2014;85(6):065115.

[13] Wu R, et al. Probability distributions of gas hydrate formation. AIChE J 2013;59(7):2640–6.

[14] May EF, et al. Quantitative kinetic inhibitor comparisons and memory effect measurements from hydrate formation probability distributions. Chem Eng Sci 2014;107:1–12.

[15] Kashchiev D, Firoozabadi A. Nucleation of gas hydrates. J Cryst Growth 2002;243(3–4):476–89.

[16] Svartaas TM, et al. Maximum likelihood estimation – a reliable statistical method for hydrate nucleation data analysis. Energy Fuels 2015;29(12):8195–207.

[17] Kashchiev D. Nucleation: basic theory with applications. UK: Butterworth-Heinemann; 2000.

[18] Jiang S, ter Horst JH. Crystal nucleation rates from probability distributions of induction times. Cryst Growth Des 2011;11(1):256–61.

[19] Kulkarni SA, et al. Crystal nucleation kinetics from induction times and metastable zone widths. Cryst Growth Des 2013;13(6):2435–40.

[20] Brandel C, ter Horst JH. Measuring induction times and crystal nucleation rates. Faraday Discuss 2015;179:199–214.

[21] Poornachary SK, et al. Crystallizing micronized particles of a poorly water-soluble active pharmaceutical ingredient: nucleation enhancement by polymeric additives. Cryst Growth Des 2016;16(2):749–58.

[22] Takeya S, et al. Freezing-memory effect of water on nucleation of CO2 hydrate crystals. J Phys Chem B 2000;104(17):4164–8.

[23] Ke W, et al. Inhibition-promotion: dual effects of polyvinylpyrrolidone (PVP) on Structure-II hydrate nucleation. Energy Fuels 2016;30(9):7646–55.

[24] Elliott C, et al. National Instruments LabVIEW: a programming environment for laboratory automation and measurement. SLAS TECHNOLOGY: Trans Life Sci Innov 2007;12(1):17–24.

[25] Van Leer B. Towards the ultimate conservative difference scheme: V. 2nd-Order sequel to godunovs method. J Comput Phys 1979;32(1):101–36.

[26] Kurganov A, Levy D. A third-order semidiscrete central scheme for conservation laws and convection-diffusion equations. Siam J Sci Comput 2000;22(4):1461–88.

[27] Yakhot V, Orszag SA. Renormalization Group Analysis of Turbulence. I. Basic Theory. J. Sci. Comput. 1986;1(1):3–51.

[28] Kato M, Launder BE. The modelling of turbulent flow around stationary and vibrating square cylinders. Kyoto, Japan: Ninth Symposium on Turbulent Shear Flows; 1993.

[29] Winter HH. Viscous dissipation term in energy equations, in calculation and measurement techniques for momentum, energy and mass transfer. New York, USA: American Institute of Chemical Engineers; 1987.

[30] MultiFlash 6.2. 2016, Infochem/KBC Advanced Technologies plc.

[31] Adamova TP, et al. Methane hydrate nucleation on water-methane and water-decane boundaries. Thermochim Acta 2018;668:178–84.

[32] Hindmarsh JP, Wilson DI, Johns ML. Using magnetic resonance to validate predictions of the solid fraction formed during recalescence of freezing drops. Int J Heat Mass Transf 2005;48(5):1017–21.

[33] Gupta AK, Zeng W-B, Wu Y. Exponential Distribution. Probability and Statistical Models: Foundations for Problems in Reliability and Financial Mathematics. Boston, MA: Birkhäuser Boston; 2010. p. 23–43.

[34] Maeda N. Nucleation curves of model natural gas hydrates on a quasi-free water droplet. AIChE J 2015;61(8):2611–7.

[35] Maeda N. Nucleation curves of methane – propane mixed gas hydrates in hydrocarbon oil. Chem Eng Sci 2016;155:1–9.

[36] Tanaka R, Sakemoto R, Ohmura R. Crystal growth of clathrate hydrates formed at the interface of liquid water and gaseous methane, ethane, or propane: variations in crystal morphology. Cryst Growth Des 2009;9(5):2529–36.

[37] Alizadeh A, et al. Dynamics of ice nucleation on water repellent surfaces. Langmuir 2012;28(6):3180–6.

[38] Makogon YF. Hydrates of hydrocarbons. Tulsa, OK, USA: PennWell Publishing Company; 1997. p. 482.

[39] Maeda N. Nucleation curves of methane hydrate from constant cooling ramp methods. Fuel 2018;223:286–93.

[40] Maeda N. Nucleation curves of methane-propane mixed gas hydrates in the presence of a stainless steel wall. Fluid Phase Equilib 2016;413:142–7.

[41] Sowa B, et al. Formation of ice, tetrahydrofuran hydrate, and methane/propane mixed gas hydrates in strong monovalent salt solutions. Energy Fuels 2014;28(11):6877–88.

[42] Englezos P, et al. Kinetics of gas hydrate formation from mixtures of methane and ethane. Chem Eng Sci 1987;42(11):2659–66.

[43] Vysniauskas A, Bishnoi PR. A kinetic-study of methane hydrate formation. Chem Eng Sci 1983;38(7):1061–72.

[44] Vysniauskas A, Bishnoi PR. Kinetics of ethane hydrate formation. Chem Eng Sci 1985;40(2):299–303.

[45] Turner D, et al. Development of a hydrate kinetic model and its incorporation into the OLGA2000 transient multi-phase flow simulator. Trondheim, Noway: Fifth International Conference on Gas Hydrates; 2005.